metals

Article

A Study on the TiC Precipitation Behavior of High-Strength Weathering Steel for Photovoltaic Supports and Its Impact on Performance

Zhiwei Liu [1,2], Xiuhua Gao [1,*], Changyou Zhu [1], Shuo Gao [3], Zhiyong Chang [1], Linxiu Du [1] and Hongyan Wu [1]

[1] State Key Laboratory of Digital Steel, Northeastern University, Shenyang 110819, China; aglzw@126.com (Z.L.); cyzhuneu@163.com (C.Z.); zychangneu@163.com (Z.C.); dulx@ral.neu.edu.cn (L.D.); wuhy@ral.neu.edu.cn (H.W.)
[2] Angang Steel Co., Ltd., Anshan 114009, China
[3] College of Information Science and Engineering, Northeastern University, Shenyang 110819, China; gaosure1993@126.com
* Correspondence: xiuhuagaoneu@126.com

Abstract

To address the strength fluctuation observed in Ti microalloyed steel, the effects of final rolling temperature, coiling temperature, and Ti content on the microstructure, secondary phase precipitation behavior, and grain size were investigated through simulation experiments. Various characterization techniques were employed to elucidate the underlying causes of the strength variation, and key control strategies were proposed. The results indicate that the strength fluctuation is primarily influenced by the presence of nano-sized TiC precipitates. The precipitation behavior of TiC can be effectively controlled by adjusting the content of non-metallic elements as well as the final rolling and coiling temperatures. Higher final rolling temperatures combined with appropriate coiling temperatures promote increased TiC precipitation; however, excessively high temperatures may result in grain coarsening and inhomogeneous precipitate distribution. The optimal processing parameters were determined to be a final rolling temperature of 860 °C and a coiling temperature of 600 °C.

Keywords: Ti microalloying; strength fluctuation; precipitated phase; final rolling temperature; coiling temperature

Academic Editor: Hardy Mohrbacher

Received: 20 April 2026
Revised: 8 May 2026
Accepted: 8 May 2026
Published: 12 May 2026

1. Introduction

With the continuous increase in global demand for renewable energy, solar photovoltaic power generation technology has been widely adopted. As a critical component in photovoltaic power generation systems, the performance of materials used for photovoltaic mounting structures has attracted significant attention. Currently, the primary materials used for photovoltaic brackets include hot-dip galvanized steel, aluminum alloy, and stainless steel [1]. However, when exposed to prolonged extreme environmental conditions such as intense sunlight, strong winds, and snow or ice, the galvanized coating of hot-dip galvanized steel is susceptible to corrosion and delamination, which can lead to serious safety risks. Although aluminum alloys offer the advantage of being lightweight, their relatively low yield strength limits their load-bearing capacity. Stainless steel, while exhibiting excellent corrosion resistance, is associated with high manufacturing costs, which hinders its widespread application [2]. Therefore, the development of novel photovoltaic bracket

materials that integrate high strength and toughness, superior corrosion resistance, and cost-effectiveness is of critical importance.

Weathering steel primarily achieves enhanced corrosion resistance through the addition of alloying elements such as Cu, Cr, and Ni [3–7], while its mechanical properties are improved via microalloying techniques involving elements like Nb, V, and Ti [8–10]. It exhibits favorable corrosion resistance and mechanical performance. However, the yield strength of currently available weathering steel typically ranges from 500 to 700 MPa, which is relatively low. Moreover, its corrosion resistance does not fully satisfy the requirements for steel materials used in photovoltaic support structures. Therefore, the development of high-strength, lightweight, durable, and economically viable weathering steel tailored for photovoltaic support applications remains a significant technical challenge [11–13].

This paper aims to address the limitations in corrosion resistance and economic efficiency of photovoltaic support structures in complex environmental conditions. To achieve this, alloying elements such as Cu, Cr, Ni, and Sb are introduced to enhance corrosion resistance, while a single Ti microalloying strategy is employed to develop an economically viable, high-strength, corrosion-resistant steel suitable for photovoltaic support structures, with a tensile strength exceeding 700 MPa. However, the addition of Ti may lead to notable fluctuations in the strength of hot-rolled steel strips, thereby complicating the structural design of photovoltaic supports. Studies on the precipitation behavior of Ti have shown a significant influence on these strength variations [14–18]. Compared to Nb and V, Ti offers a more pronounced strengthening effect at a lower cost. In steel, Ti primarily exists in the form of precipitates such as TiN, TiC, $Ti_4C_2S_2$, TiO, and TiS [19], among which TiC particles can be as small as 10 nm and are considered the primary contributor to strengthening [20,21]. Mao et al. successfully obtained nano-sized TiC precipitates through Ti microalloying, achieving a yield strength of 730 MPa [12]. Peng et al. reported that the TiC content significantly influences the material's strength; the yield stress of steel subjected to isothermal treatment with a higher TiC content increased by 211 MPa compared to that of air-cooled steel [11].

Although Ti exhibits a significant strengthening effect, Ti microalloyed steels are characterized by a complex variety of second-phase types and a broad precipitation temperature range. During the production process, this complexity can lead to an uneven distribution of precipitates, which may result in variations in strength across different steel coils or within different regions of the same coil [22,23]. Research has shown that the precipitation behavior of Ti is primarily influenced by the final rolling temperature and coiling conditions [24,25]. Ti precipitates can form through various mechanisms, including interphase precipitation, dispersion precipitation, and deformation-induced precipitation. These mechanisms are predominantly governed by the final rolling temperature; higher final rolling temperatures generally promote a greater volume of precipitates [26–28]. According to the research by Natarajan et al., appropriately increasing the coiling temperature can enhance precipitate formation. However, excessively high coiling temperatures may lead to grain coarsening, which is detrimental to grain refinement strengthening [25]. Similarly, Patra et al. reported that raising the coiling temperature from 520 °C to 580 °C increases both the number of precipitates and dislocation density, resulting in a 50 MPa improvement in yield strength [29].

The microalloying regulation mechanism of weathering steel used in photovoltaic support structures has been extensively investigated. However, the currently used single Ti microalloyed steel still faces challenges, including generally low strength, unclear Ti precipitation behavior, and the mechanism underlying strength fluctuations. To address these issues, an ultra-high-strength weathering steel for photovoltaic support applications with varying Ti contents was designed in this study. The effects of final rolling temperature

and coiling temperature on the precipitation behavior of the second phase and microstructural evolution were analyzed through thermodynamic calculations and hot simulation experiments. Based on these findings, the precipitation-strengthening mechanism and the mechanism responsible for strength fluctuations were proposed and validated through pilot rolling experiments. This research provides a solid theoretical foundation and valuable reference for the development and production of next-generation lightweight weathering steels for photovoltaic support systems.

2. Materials and Methods

2.1. Experimental Materials

In this study, the low-C principle was applied, and corrosion-resistant alloying elements such as Cr, Ni, Cu, and Sb were added in appropriate proportions to develop weathering steels with varying Ti contents. The chemical compositions of the designed steels are summarized in Table 1.

Table 1. Chemical composition of Ti microalloyed corrosion-resistant steel (mass%).

Steels	C	Si	Mn	P	S	Als	Cu	Ni	Cr	Sb	Ti
NS1	0.063	0.251	1.01	0.004	0.002	0.021	0.290	0.151	0.92	0.087	0.140
NS2	0.060	0.250	1.03	0.004	0.002	0.024	0.30	0.157	0.91	0.083	0.062

2.2. Thermal Simulation Experiment

Thermal simulation experiments were conducted using the MMS 200 thermal simulation testing machine (Northeastern University, Shenyang, China) to simulate the hot rolling process of NS1 steel. The specimens used in the experiments were cylindrical with a diameter of 5 mm and a length of 15 mm.

To investigate the effect of final rolling temperature on the precipitation behavior of the secondary phase, the samples were first heated to 1200 °C at a rate of 10 °C/s and held for 300 s. They were then cooled at a rate of 10 °C/s to 1050 °C, followed by single-pass compression deformation with a reduction of 6 mm. Subsequently, the samples were cooled at the same rate to different target temperatures (800, 830, 860, and 890 °C) and subjected to another single-pass compression with a reduction of 4 mm. The strain rate during compression was maintained at 5 mm/s. After deformation, the samples were cooled at a rate of 20 °C/s to 600 °C and then at a slower rate of 0.1 °C/s to room temperature to simulate the coiling process. The experimental procedure is illustrated in Figure 1a.

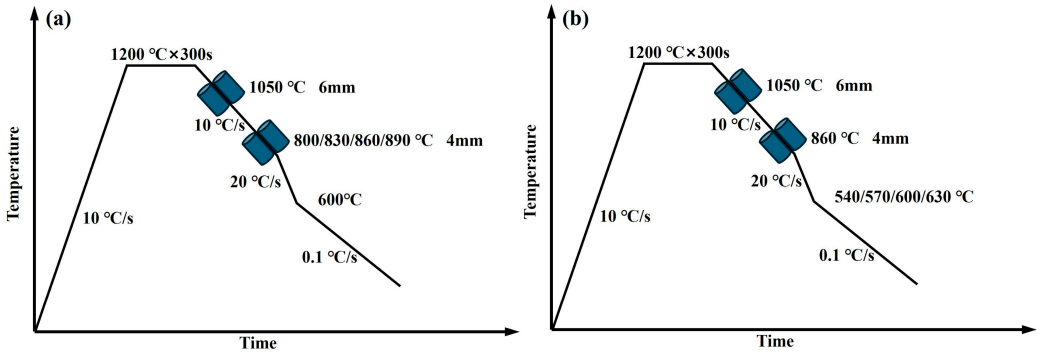

Figure 1. Thermal simulation process diagram of corrosion-resistant steel: (**a**) experimental processes with different final rolling temperatures; (**b**) experimental processes at different coiling temperatures.

To investigate the effect of coiling temperature on the precipitation behavior of the secondary phase, after the first pass of compression, the sample was cooled at a rate of 10 °C/s to 860 °C for single-pass compression deformation, which simulated the finish rolling process, with a reduction of 4 mm. The strain rate during compression was maintained at 5 mm/s. Following deformation, the sample was subsequently cooled at a rate of 20 °C/s to various target temperatures (540, 570, 600, and 630 °C) and then cooled at a slower rate of 0.1 °C/s to room temperature to simulate the coiling process. The corresponding thermal processing schedule is illustrated in Figure 1b.

2.3. Microstructure Characterization

The specimen was sectioned at a location 1 mm below the thermocouple of the thermal simulation specimen, along a direction perpendicular to the deformation direction. Following polishing of the cross-sectional surface, the specimen was etched using a 4 vol.% nitric acid alcohol solution for approximately 30 s. Subsequently, the microstructure was examined using a ZEISS Ultra55 field emission scanning electron microscope (SEM) (ZEISS, Oberkochen, Germany).

A 500 μm thick cross-sectional slice was cut perpendicular to the deformation direction, located 1 mm below the thermocouple. The specimen was first mechanically polished to a thickness of approximately 45 μm and subsequently subjected to double-jet electropolishing in a solution containing 9 vol.% perchloric acid in ethanol at a temperature of −23 °C and a voltage of 28 V. The size, morphology, and spatial distribution of the precipitated particles were analyzed using a Tecnai G2 F20 transmission electron microscope (TEM) (FEI, Hillsboro, OR, USA).

Electrolytic polishing was carried out using an ElectroMetTM4 Polisher Etcher electrolytic polisher (Buehler, Lake Bluff, IL, USA). The electrolytic polishing solution was a mixture of perchloric acid and anhydrous ethanol (1:7), and the electrolytic polishing parameters were 20 V for 20 s. Subsequently, EBSD analysis was conducted using a ZEISS Ultra55 field emission scanning electron microscope.

2.4. Mechanical Performance Test

The micro-Vickers hardness of the sample was measured using an FM-700 microhardness tester (Future-Tech Corp, Kawasaki, Japan) under a load of 300 gf and a loading time of 10 s. The tensile test was conducted at room temperature using a 5105-SANS electronic universal tensile testing machine (Sans, Shenzhen, China) at a tensile speed of 3 mm/min.

2.5. Hot Rolling Experiment

Forged square billets with a thickness of 80 mm were homogenized at 1200 °C for 2 h in a heating furnace. Then, they were hot-rolled to a thickness of 3 mm in two stages using a Φ450 mm two-high reversible rolling mill (Northeastern University, Shenyang, China), with reduction rates of 76% and 84% for rough rolling and finish rolling, respectively. After rolling, the steel plates were sprayed with water to cool to different temperatures and then cooled to room temperature in the furnace.

3. Results

3.1. Equilibrium Phase Diagrams with Different Ti Contents

The equilibrium phase diagrams of weathering steels with varying Ti contents, calculated using JMatPro thermodynamic simulation software (Sente, Guildford, UK), are presented in Figure 2. As the Ti content increases from 0.062% to 0.140%, the phase transformation temperatures Ac_1 and Ac_3 rise from 712 °C and 847 °C to 715 °C and 854 °C, respectively. Ti is a strong carbide-forming element that preferentially reacts with carbon to

form stable TiC, thereby decreasing the concentration of free carbon in the matrix. Since the formation of austenite depends on the dissolution of carbon atoms, the reduced carbon activity results in lower carbon solubility in ferrite. Consequently, a higher temperature is required to achieve the necessary carbon concentration for austenite nucleation, which leads to an increase in the phase transformation temperatures.

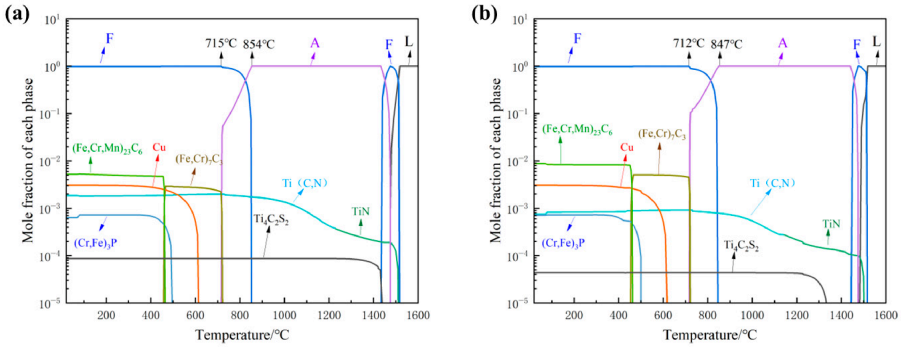

Figure 2. The equilibrium phase diagram of the experimental steel: (**a**) NS1; (**b**) NS2.

As the precipitation temperature decreases, the primary precipitated phases in the NS1 and NS2 weathering steels include TiN, $Ti_4C_2S_2$, Ti(C,N), M_7C_3, Cu, M_3P, and $M_{23}C_6$ [30]. Notably, the commonly observed MnS phase in conventional steels did not form in the experimental steel. This is attributed to the higher thermodynamic stability and formation tendency of Ti sulfides and carbides compared to MnS. The absence of large-sized MnS inclusions, which are detrimental to the overall mechanical properties of the steel, is beneficial for enhancing the material's comprehensive mechanical performance.

3.2. The Influence of Final Rolling Temperature on Microstructure

3.2.1. Microstructure

The microstructure and Vickers hardness of NS1 steel at a coiling temperature of 600 °C and various final rolling temperatures were investigated through thermal simulation experiments, as presented in Figures 3 and 4, respectively. Based on the analysis of microhardness and morphological features, the microstructure under different final rolling temperatures was identified as polygonal ferrite combined with granular bainite. Furthermore, it was observed that the grain size of NS1 steel decreased with decreasing final rolling temperature. This phenomenon can be attributed to the higher dislocation density retained in the steel at lower final rolling temperatures, which provides more nucleation sites for subsequent phase transformations, inhibits grain growth, and thereby contributes to grain refinement [31–33].

3.2.2. Precipitation Morphology

The Ti element initially forms compounds with O, N, and S elements present in the steel. Any remaining Ti subsequently combines with C. When sufficient carbon is available in the steel, the solubility of Ti is directly proportional to the temperature. The solubility of Ti in austenite can be described by Equation (1) [34]:

$$\log([\mathrm{Ti}][\mathrm{C}]) = 3.21 - 7489/T \quad (1)$$

According to the calculations, when the final rolling temperature is 800 °C, the maximum solid solubility of Ti in the weathering steel is approximately 0.056%. When the final rolling temperature increases to 860 °C, the maximum solid solubility of Ti rises to approximately 0.081%, and at 890 °C, it reaches approximately 0.098%. These results indicate that as the final rolling temperature increases, the solid solubility of Ti in the

steel also increases, leading to a greater number of fine TiC precipitates formed during the subsequent coiling process. This phenomenon enhances precipitation strengthening in the steel. The morphology of the precipitated phases in NS1 steel at different final rolling temperatures is presented in Figure 5. It can be observed that the number of precipitated phases at 860 °C is significantly higher than that at 800 °C. Therefore, within the temperature range of 800~860 °C, the increase in Vickers hardness with increasing final rolling temperature is primarily attributed to precipitation strengthening [35]. However, when the final rolling temperature increases further from 860 to 890 ° C, the decrease in Vickers hardness is mainly due to the effect of fine-grain strengthening [36].

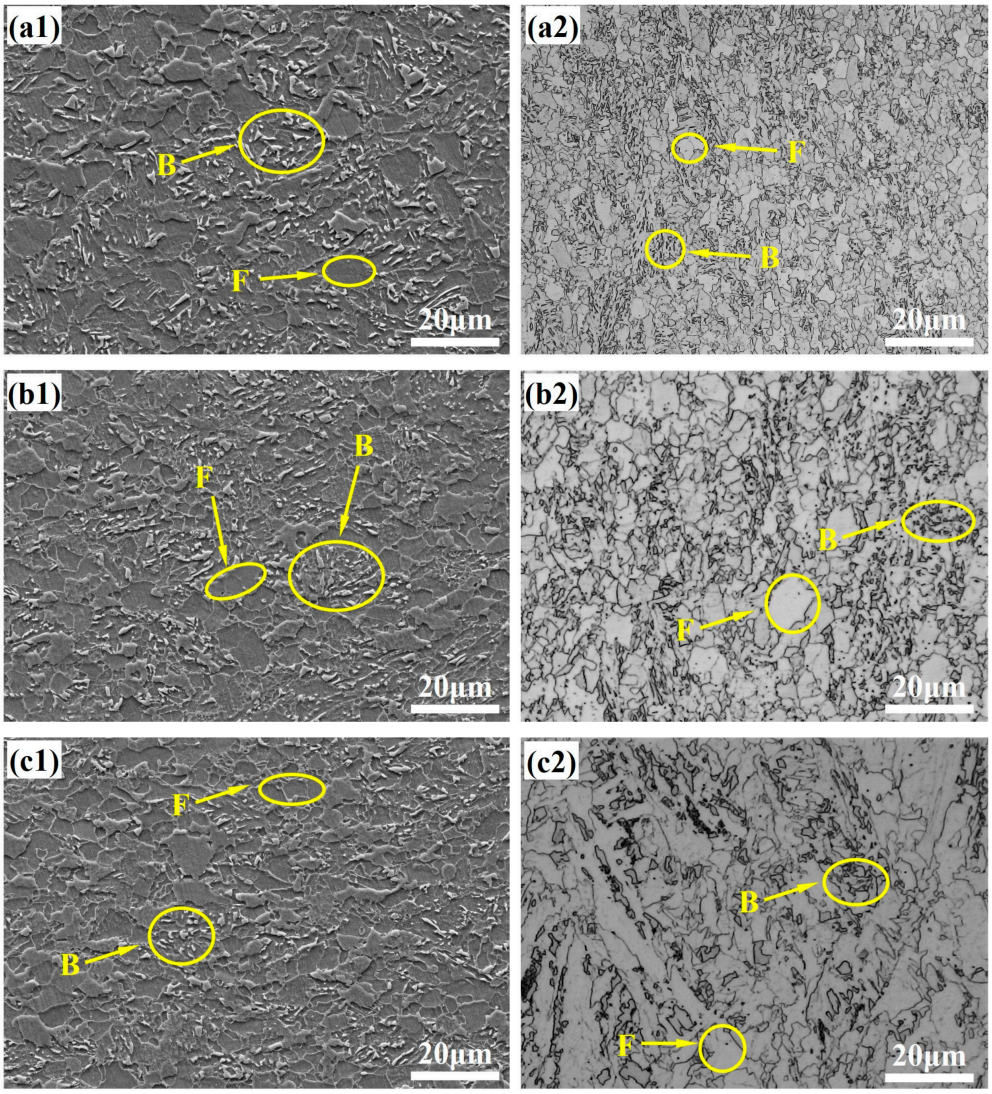

Figure 3. Microstructure of NS1 at different final rolling temperatures: (**a1**,**a2**) 800 °C; (**b1**,**b2**) 830 °C; (**c1**,**c2**) 890 °C. F represents ferrite, and B represents bainite.

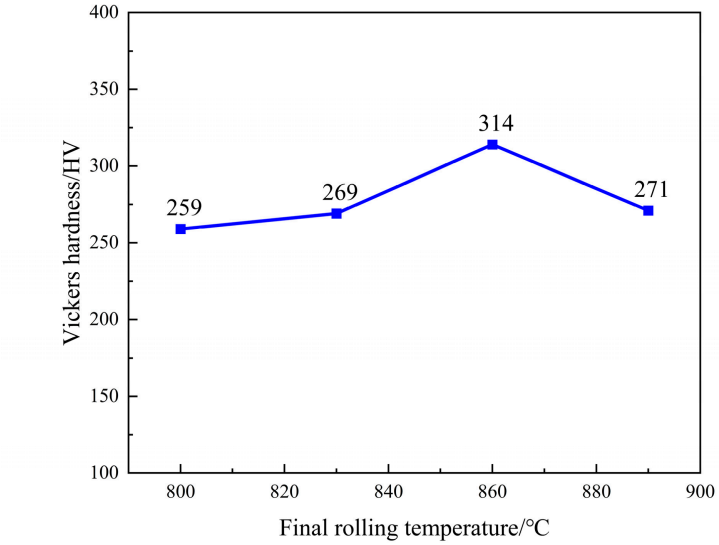

Figure 4. The variation law of Vickers hardness at different final rolling temperatures.

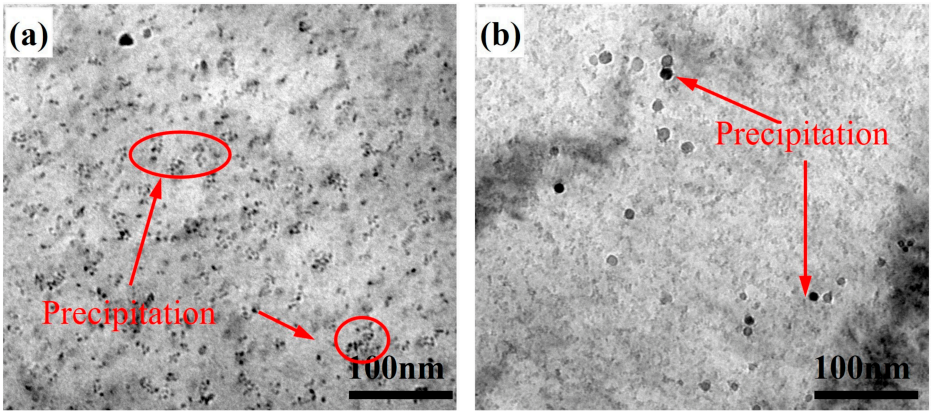

Figure 5. Morphology of precipitated phases at different final rolling temperatures: (**a**) 860 °C; (**b**) 800 °C.

3.3. The Influence of Curling Temperature on Microstructure

3.3.1. Microstructure

The microstructure of NS1 steel at the final rolling temperature of 860 °C and various coiling temperatures is presented in Figure 6. When the coiling temperature is set at 540 °C, the microstructure of NS1 steel, as shown in Figure 6(a1,a2), is predominantly composed of granular bainite with a minor amount of polygonal ferrite. This can be attributed to the relatively large undercooling at this stage, leading to a transformation of the transitional type. At a coiling temperature of 570 °C (Figure 6(b1,b2)), it can be observed that with the increase in coiling temperature, more austenite undergoes diffusion-type transformation. Consequently, the bainite content in the microstructure increases, while the ferrite content decreases. When the coiling temperature reaches 600 °C (Figure 6(c1,c2)), the ferrite content surpasses that of bainite in the microstructure. Further increasing the coiling temperature to 630 °C (Figure 6(d1,d2)) results in a microstructure primarily consisting of polygonal ferrite with a small proportion of pearlite [37].

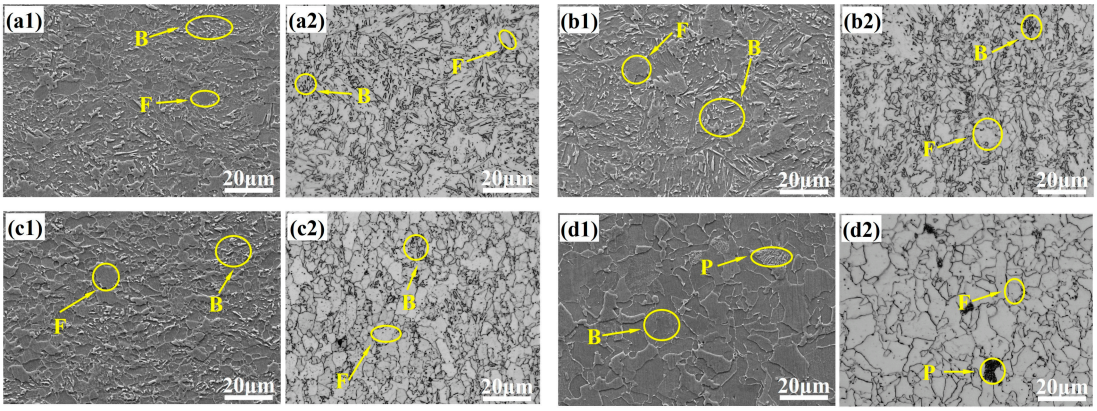

Figure 6. Microstructure of NS1 at different coiling temperatures: (**a1**,**a2**) 540 °C; (**b1**,**b2**) 570 °C; (**c1**,**c2**) 600 °C; (**d1**,**d2**) 630 °C. F represents ferrite, B represents bainite, and P represents Pearlite.

The variation law of Vickers hardness of NS1 steel under different thermal simulation processes is shown in Figure 7. When the final rolling temperature is set at 860 °C and the coiling temperature falls within the range of 540~630 °C, the Vickers hardness of the steel exhibits an initial increasing trend followed by a decrease. The maximum Vickers hardness is achieved when the coiling temperature is 600 °C.

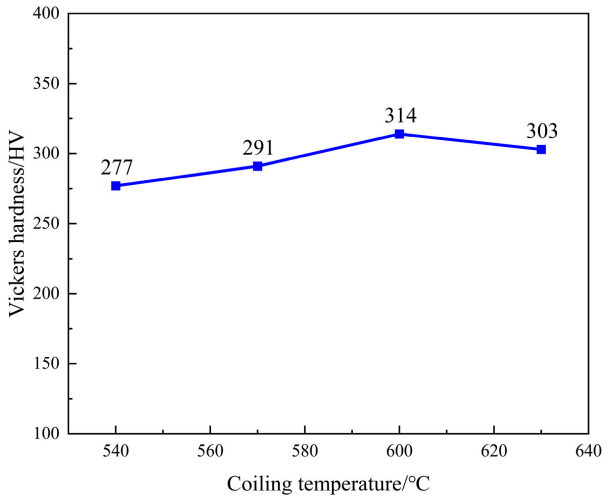

Figure 7. Vickers hardness of NS1 steel at different coiling temperatures.

The inverse pole figure (IPF) diagrams of NS1 steel at various coiling temperatures are presented in Figure 8. When the coiling temperatures are set at 540, 570, 600, and 630 °C, respectively, the corresponding grain sizes of the NS1 steel are measured as 2.31, 3.21, 3.34, and 3.45 μm. With the increase in coiling temperature, the grain size exhibits a gradual upward trend. This phenomenon can be attributed to the fact that higher coiling temperatures supply greater thermal energy, which promotes grain growth [38].

The strengthening effect resulting from grain refinement is described by the Hall-Petch equation, as presented in Equation (2). Among various strengthening mechanisms, grain refinement is unique in that it simultaneously improves both the strength and toughness of materials. Grain refinement can be achieved through several approaches, including refining austenite grains or introducing dislocations prior to phase transformation, promoting nucleation sites within austenite, and controlling grain size during phase transformation cooling. The grain size can be effectively regulated by optimizing the hot rolling process [39]. Due to the differing crystallographic orientations among adjacent grains, microcracks encounter significant resistance when propagating across grain boundaries. Upon traversing a grain,

the crack propagation direction changes, which further impedes fracture. As grain size decreases, the number of grain boundaries increases, leading to a greater number of grains with varying orientations that must be accommodated during deformation. Consequently, higher energy is required for microcrack propagation, coalescence, and ultimate material failure, which is macroscopically observed as an enhancement in material strength.

$$\sigma_g = k_y d^{-\frac{1}{2}} \quad (2)$$

where σ_g denotes the contribution of fine-grain strengthening; d denotes the average grain size in millimeters; k_y denotes the proportionality coefficient. For steel materials, its value ranges from 14.0 to 23.4 MPa·mm$^{1/2}$, and in low-carbon steel, 17.4 MPa·mm$^{1/2}$ is commonly adopted.

As the coiling temperature of NS1 steel increases from 540 °C to 630 °C, the grain size increases from 2.31 μm to 3.45 μm, σ_g decreases from 362 MPa to 295 MPa, and the contribution of fine grain strengthening drops by 67 MPa.

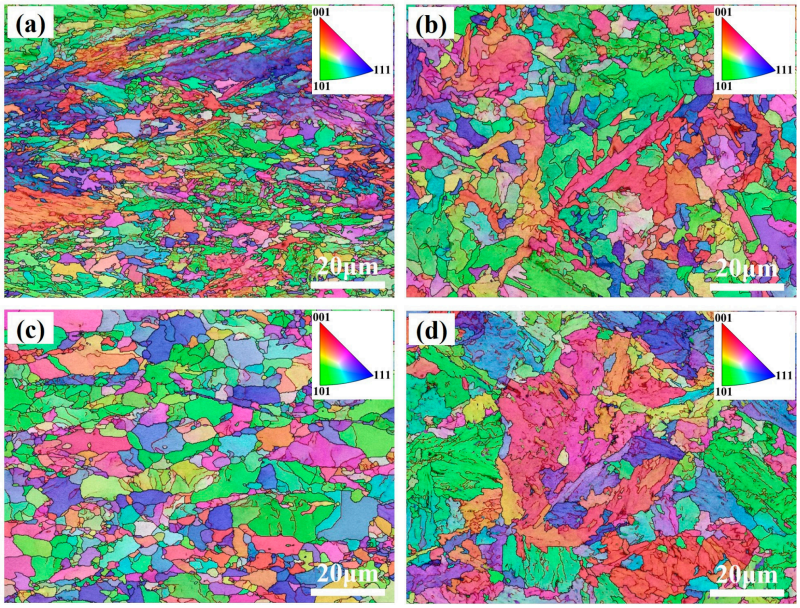

Figure 8. IPF maps of NS1 at different coiling temperatures: (**a**) 540 °C; (**b**) 570 °C; (**c**) 600 °C; (**d**) 630 °C.

3.3.2. Precipitation Morphology

The variation in Vickers hardness at different coiling temperatures can be attributed to the combined effects of grain refinement strengthening and precipitation strengthening. Figure 9 presents the morphology and elemental composition of the precipitated phases in NS1 steel at coiling temperatures of 540 °C and 600 °C. At 540 °C, only a limited number of precipitated phases are observed, with all of them exceeding 10 nm in size. In contrast, at 600 °C, in addition to a few large precipitated phases, numerous fine precipitates are dispersed throughout the microstructure.

The second-phase precipitates can be categorized into two distinct types based on the temperature ranges at which they form. The first type develops during the rolling process. This occurs because plastic deformation generates a significant number of dislocations, which in turn promote the nucleation of the second phase. Due to the relatively high precipitation temperature associated with this type, the resulting precipitates are comparatively large in size [40,41]. The second type forms during the coiling process. As the temperature decreases, the solubility of alloying elements diminishes. When the concentration of these elements exceeds their maximum solubility through diffusion, they precipitate uniformly

within the ferrite matrix [42]. This type of precipitation occurs at a lower temperature, leading to finer precipitate particles that provide a pronounced precipitation-strengthening effect [43].

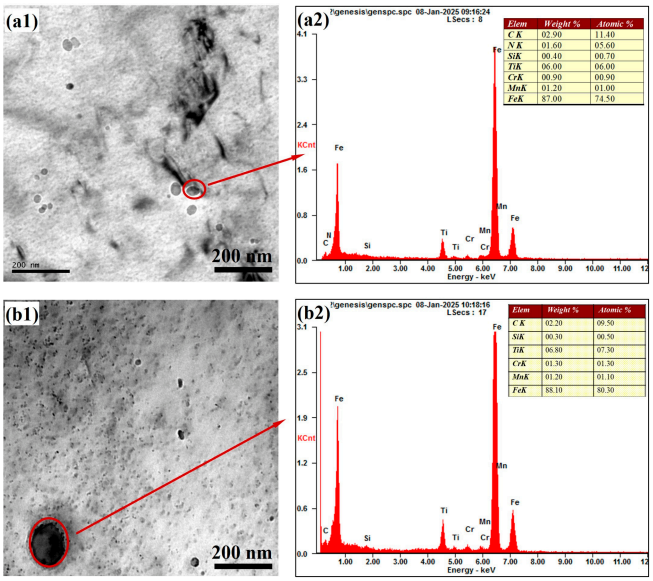

Figure 9. Morphology and elemental composition of the precipitated phases of NS1 at different coiling temperatures: (**a1**,**a2**) 540 °C; (**b1**,**b2**) 600 °C.

When the coiling temperature is 540 °C, the relatively low temperature results in limited diffusion capability of the alloying elements, making it difficult to precipitate and form compounds during the coiling process. Consequently, only a small quantity of large-sized precipitates, primarily induced by deformation, is present. In contrast, when the coiling temperature is increased to 600 °C, the elevated temperature provides sufficient energy to promote nucleation, while the slower cooling rate during coiling allows ample time for precipitation. As a result, numerous fine precipitates are uniformly dispersed within the ferrite matrix [44]. According to the energy-dispersive X-ray spectroscopy analysis of precipitates in NS1 steel, the primary precipitates at 540 °C are TiC and TiN, whereas TiC is predominantly observed at 600 °C. Based on the statistical analysis of 20 representative transmission electron microscopy (TEM) images, the average precipitate sizes at coiling temperatures of 540 °C and 600 °C are 11.34 nm and 3.67 nm, respectively. The corresponding average precipitate spacings are calculated to be 276 nm and 48 nm, respectively.

The volume fraction and size of the secondary phase are the primary factors that influence its strengthening effect. Dislocations in steel interact with the secondary phase, thereby impeding their movement [45]. When dislocations bypass non-deformable secondary phase particles, the relationship between the increase in strength and the volume fraction, as well as particle size, is described by Equations (3) and (4).

$$\sigma_p \propto f^{\frac{1}{2}} d^{-1} ln d \tag{3}$$

$$\sigma_p = 0.298 \frac{\mu b}{l} ln\left(\sqrt{\frac{2}{3}} \times \frac{d}{\mathrm{b}}\right) \tag{4}$$

where σ_p denotes the contribution of precipitation strengthening, MPa; f denotes the volume fraction of the second phase, %; d denotes the diameter of the precipitated particles in nanometers, nm; μ denotes the shear modulus, which is taken as 8×10^4 MPa; b denotes the Burgers vector of dislocations with a value of 2.5×10^{-7} mm; l denotes the spacing between precipitates, nm. Calculations indicate that when the coiling temperature is set to

540 °C and 600 °C, the increments of precipitation strengthening are 78 MPa and 226 MPa, respectively. These results suggest that an increase in coiling temperature significantly enhances the precipitation-strengthening effect.

3.4. The Influence of Ti Content on Microstructure

The microstructure of NS2 steel under varying final rolling and coiling temperatures is presented in Figure 10. In comparison with NS1 steel, a reduction in Ti content from 0.15% to 0.07% does not alter the microstructural type, which remains composed of granular bainite, ferrite, and a minor amount of pearlite.

The variation in the Vickers hardness of NS2 steel under different thermal simulation processes is shown in Figure 11. When the final rolling temperature is maintained at 860 °C, and the coiling temperature ranges between 540 °C and 630 °C, the Vickers hardness of NS2 steel initially increases and subsequently decreases, reaching its maximum value at a coiling temperature of 600 °C. Conversely, when the coiling temperature is fixed at 600 °C, and the final rolling temperature varies between 800 °C and 890 °C, the Vickers hardness remains relatively stable with no significant variation. The overall Vickers hardness of NS2 steel is lower than that of NS1 steel, which can be attributed to a reduction in Ti content from 0.15% to 0.07%, thereby weakening the effects of precipitation strengthening and grain refinement strengthening [44,46].

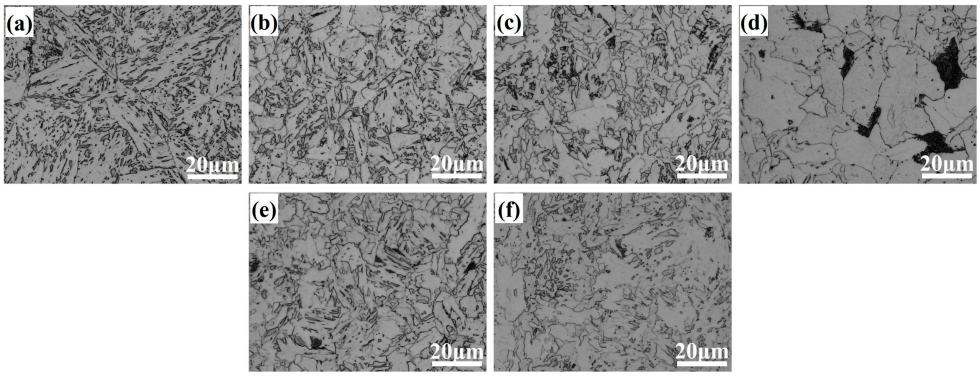

Figure 10. Microstructure of NS2 under different thermal simulation processes: (**a**) final rolling temperature: 860 °C, coiling temperature: 540 °C; (**b**) final rolling temperature: 860 °C, coiling temperature: 570 °C; (**c**) final rolling temperature: 860 °C, coiling temperature: 600 °C; (**d**) final rolling temperature: 860 °C, coiling temperature: 630 °C; (**e**) final rolling temperature: 800 °C, coiling temperature: 600 °C; (**f**) final rolling temperature: 830 °C, coiling temperature: 600 °C.

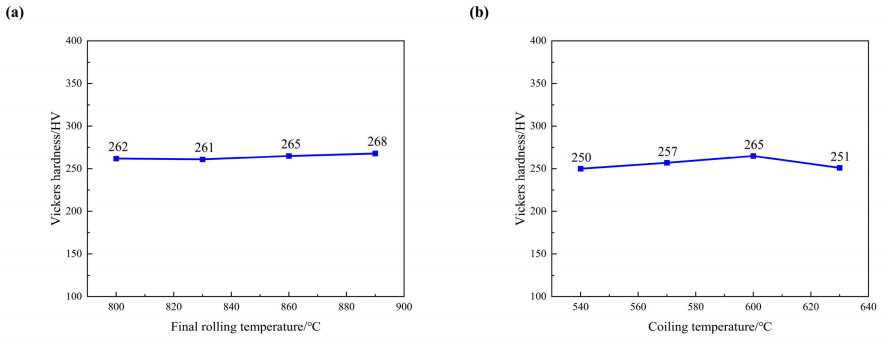

Figure 11. Vickers hardness of NS2 steel under different thermal simulation processes: (**a**) different coiling temperatures; (**b**) different final rolling temperatures.

The variation range of Vickers hardness in NS2 steel is smaller than that of NS1 steel with changes in coiling temperature. This can be attributed to the reduced Ti content in NS2 steel, which decreases the solid solubility of Ti during the coiling process, thereby diminishing the influence of coiling temperature on the material's hardness. Changes in the final rolling temperature, however, have minimal effect on the Vickers hardness of NS2 steel. This is because, at 800 °C, the maximum solid solubility of Ti in NS2 steel reaches approximately 0.056%, which is nearly equivalent to the actual Ti content added. Consequently, an increase in the final rolling temperature does not significantly alter the solid solubility of Ti, resulting in a relatively minor impact on the Vickers hardness.

When the coiling temperature is set at 600 °C, and the final rolling temperature is 860 °C, the morphology and elemental composition of the precipitated phases in NS1 and NS2 steels were analyzed, and the results are presented in Figure 12. As shown in the figure, NS1 steel, which contains a higher Ti content, exhibits a greater number of precipitates compared to NS2 steel, thereby contributing more significantly to precipitation strengthening. The elemental composition of the secondary phase precipitates in NS2 corrosion-resistant steel, as shown in Figure 12c,d, primarily consists of Ti, C, and N [47].

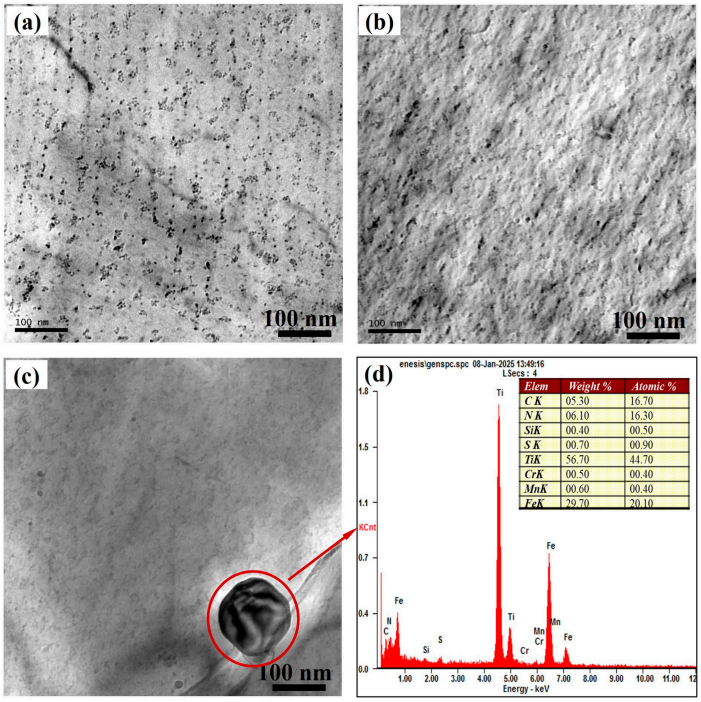

Figure 12. Morphology and elemental composition of precipitated phases in corrosion-resistant steels with different compositions: (**a**) morphology of the NS1 precipitated phase; (**b**,**c**) morphology of the NS2 precipitated phase; (**d**) elemental composition of the NS2 precipitated phase.

4. Discussion

4.1. Strengthening Mechanism

The strengthening mechanism of NS1 steel was investigated through actual rolling experiments. The microstructures of NS1 steel under different rolling processes are presented in Figure 13. The microstructures of NS1-1, NS1-2, and NS1-3 corrosion-resistant steels consist of ferrite and granular bainite. When the final rolling temperature is 916 °C, the polygonal ferrite grain size ranges approximately from 5 to 15 μm, with non-uniform grain sizes and uneven distribution. As the final rolling temperature decreases, the ferrite morphology transitions from polygonal to acicular ferrite, and the grain size is reduced. This phenomenon can be attributed to the increased stored energy within the grains caused

by the lower rolling temperature, which inhibits austenite recrystallization and refines austenite grains, thereby creating favorable conditions for subsequent ferrite transformation. NS1-3, NS1-4, and NS1-5 steels represent the microstructural variations in the experimental steel under the same final rolling temperature but different coiling temperatures. As observed in the figure, a decrease in coiling temperature leads to a significant refinement of the grain structure. Lower coiling temperatures increase the cooling rate, reduce the diffusivity of carbon atoms, and hinder the ferrite transformation process, resulting in a decrease in the relative proportion of ferrite and an increase in bainite content. Within the granular bainite of NS1 steel, numerous granular carbides are dispersed throughout the massive or acicular ferrite matrix. Granular bainite contributes to the strengthening of the steel as a second phase, while the massive ferrite matrix ensures the material's ductility and toughness. Consequently, a higher number of carbide particles correlates with increased yield and tensile strengths of the granular bainite.

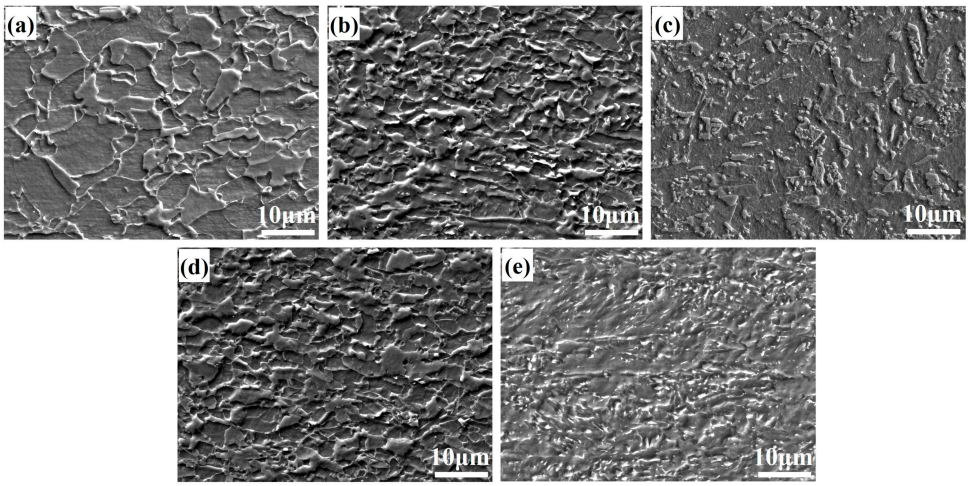

Figure 13. Microstructure of experimental steel under different rolling processes: (**a**) final rolling temperature: 916 °C, coiling temperature: 600 °C; (**b**) final rolling temperature: 866 °C, coiling temperature: 600 °C; (**c**) final rolling temperature: 840 °C, coiling temperature: 600 °C; (**d**) final rolling temperature: 860 °C, coiling temperature: 620 °C; (**e**) final rolling temperature: 860 °C, coiling temperature: 570 °C.

The mechanical properties of NS1 steel under different rolling processes are presented in Table 2 and Figure 14. With a decrease in the final rolling temperature, the yield strength and tensile strength of NS1 steel increase, while the elongation exhibits a slight reduction. This phenomenon can be attributed to the fact that lowering the final rolling temperature enhances the internal stored energy of the grains and suppresses the recrystallization behavior of austenite, thereby refining the austenite grains and creating favorable conditions for subsequent ferrite phase transformation. Consequently, the ferrite grains are significantly refined. The transformation temperature also exerts a notable influence on the microstructure of bainite, which in turn plays a crucial role in determining its mechanical properties. The presence of numerous granular carbides distributed within the granular bainite enhances the second-phase strengthening effect, thereby contributing to the overall increase in yield strength and tensile strength of the experimental steel. As the coiling temperature decreases, the elongation of NS1 steel diminishes, while the yield strength gradually increases. This is primarily due to the grain refinement induced by the reduced coiling temperature, a decrease in pearlite content, and an increase in granular bainite content, which enhances the strength of the steel but negatively affects its elongation.

Table 2. Hot rolling process parameters and mechanical properties of experimental steels.

Steels	Final Rolling Temperature/°C	Coiling Temperature/°C	Mechanical Properties			
			Yield Strength/MPa	Tensile Strength/MPa	Yield-to-Strength Ratio	Elongation Rate/%
NS1-1	916	600	697	855	0.82	18.0
NS1-2	866	600	815	885	0.92	17.5
NS1-3	840	600	818	898	0.93	13.3
NS1-4	860	620	779	877	0.89	18.1
NS1-5	860	570	829	928	0.89	13.8

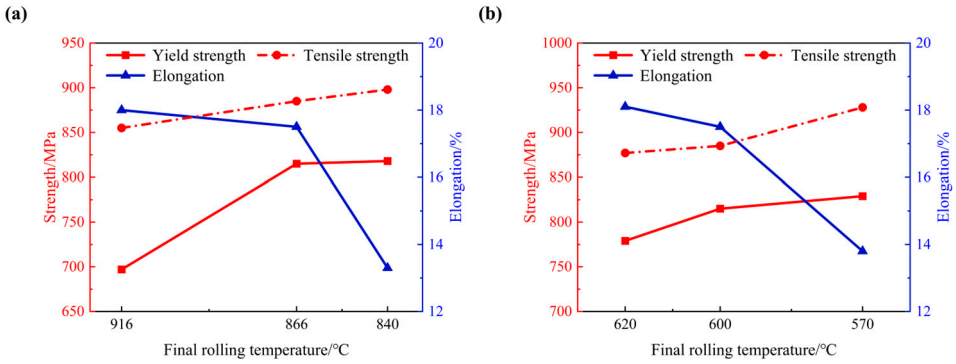

Figure 14. Comparison of mechanical properties of experimental steels: (**a**) different final rolling temperatures; (**b**) different coiling temperatures.

Under the same final rolling temperature, a lower coiling temperature enhances the strength of steel but reduces its elongation. Through a comparative analysis of the mechanical properties of the experimental steel at varying coiling temperatures, it was found that NS1 steel achieved optimal performance at a coiling temperature of 600 °C. At this temperature, the yield strength and tensile strength were 815 MPa and 885 MPa, respectively, with an elongation of 17.5%. The corresponding final rolling temperature was 866 °C, and the coiling temperature was 600 °C. The optimal process parameters for NS1-2 steel were consistent with those identified in the aforementioned thermal simulation experiment.

To further investigate the strengthening mechanism of NS1-2 steel, the morphology of precipitated phases is presented in Figure 15. As observed from the figure, the steel contains precipitates of varying sizes, both large and small, which are approximately elliptical in shape. The smaller precipitates are predominantly composed of Fe and C and may include Fe_3C or complex carbides containing Ti, Cr, and Mn. In contrast, the larger precipitates primarily consist of Fe, Ti, and C and are likely to be TiC. This observation aligns with the simulation results presented in the aforementioned content, where TiC was identified as the main precipitated phase in the experimental steel when the coiling temperature was set at 600 °C.

Twenty representative TEM images were taken, and the size and spacing of the precipitated phases were statistically analyzed using Image-Pro Plus 6.0 software (Media Cybernetics, Rockville, MD, US). The average size of the precipitated phases was 4.87 nm, and the calculated spacing of the precipitates was 62 nm. According to Formulas (3) and (4), the precipitation strengthening increment of NS1-2 steel was calculated to be 265 MPa, and the contribution of fine-grain strengthening was 306 MPa. It can be seen that the excellent strength performance of NS1-2 steel is the result of the combined effect of fine-grain strengthening and precipitation strengthening. The coordinated cooperation of multiple strengthening methods makes the performance of NS1-2 experimental steel the best.

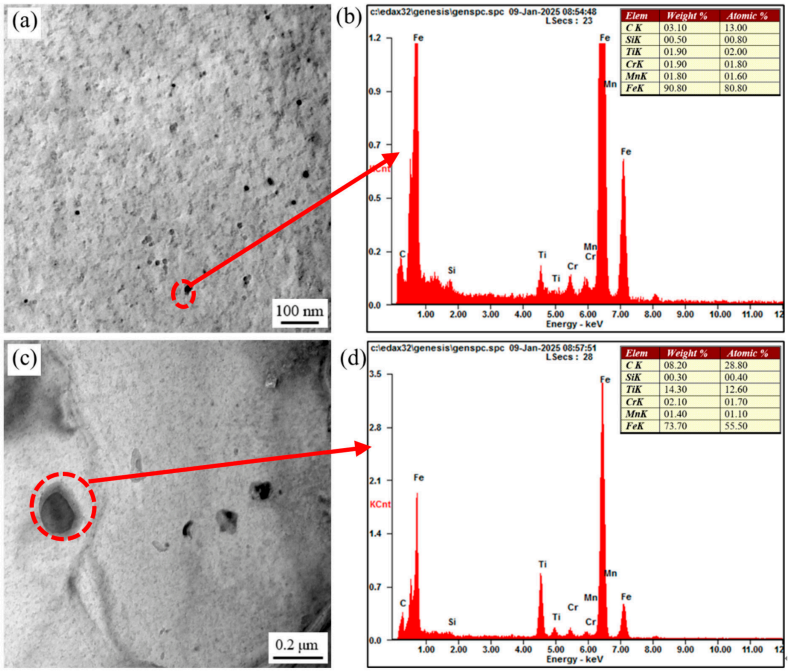

Figure 15. Morphology and elemental composition of precipitated phases in NS1-3 steel: (**a**,**b**) fine-sized precipitated phase; (**c**,**d**) large-sized precipitated phase.

4.2. Mechanism of Intensity Fluctuation

The strength fluctuation observed in Ti-microalloyed weathering steel is influenced by multiple factors. Variations in the content of N, O, and S can lead to fluctuations in the steel's strength. This occurs because the compounds formed between Ti and these non-metallic elements (O, N, and S) precipitate prior to TiC. Consequently, fluctuations in the levels of non-metallic elements affect the amount of TiC precipitate formed, which in turn influences the mechanical properties of the steel. Therefore, during composition design, it is essential to ensure that an adequate amount of Ti remains available to react with C after forming compounds with O, N, and S. This ensures the formation of a large number of finely dispersed TiC precipitates during the subsequent coiling process.

The variation in the final rolling temperature can lead to fluctuations in the mechanical strength of weathering steel. As the Ti element content decreases, the mechanical properties of the steel become more stable. Unlike other steel grades with different compositional systems, the final rolling temperature of Ti-microalloyed corrosion-resistant steel not only influences grain size but also affects the solid solution content of Ti, which in turn has a significant impact on the overall mechanical properties. Therefore, the final rolling temperature should not be set too low. An appropriately increased final rolling temperature facilitates the formation of TiC precipitates. At the same time, excessively high temperatures should be avoided to prevent grain coarsening. Based on this study, the optimal final rolling temperature is determined to be 860 °C.

The variation in coiling temperature can also lead to fluctuations in the strength of weathering steel. The Ti element is highly sensitive to precipitation temperature. Research has shown that when the coiling temperature is below 540 °C, TiC precipitation is difficult to achieve. However, when the coiling temperature exceeds 630 °C, although TiC does precipitate, it may result in grain coarsening and the formation of a pearlite structure, which is detrimental to corrosion resistance. Therefore, in practical production processes, variations in coiling temperature significantly influence the mechanical properties of corrosion-resistant steel. This study concludes that the optimal coiling temperature for corrosion-resistant steel is 600 °C.

In conclusion, the most significant factors influencing strength fluctuations are the morphology, quantity, and distribution of precipitates. Taking the analysis results of precipitate morphology under different rolling processes presented in Section 4.1 into account, the optimal production process for NS1 steel is determined to involve a final rolling temperature of 860 °C and a coiling temperature of 600 °C.

5. Conclusions

This paper involves an in-depth study on the strengthening mechanism of high-strength weathering steel used for photovoltaic support, clarifies the precipitation law of the second phase, identifies the mechanism of strength fluctuation, and proposes key control measures. The main conclusions are as follows:

(1) When the final rolling temperature ranges between 800 and 890 °C, an increase in the final rolling temperature results in a rise in the content of dissolved Ti from 0.056% to 0.081%. Consequently, the number of precipitated phases in NS1 steel increases, with TiC being the dominant precipitated phase. This phenomenon leads to an increase in the Vickers hardness of NS1 steel, from 259 HV to 314 HV.

(2) With the increase in coiling temperature, the Vickers hardness of NS1 steel exhibits a trend of initial increase followed by a decrease. At a coiling temperature of 540 °C, only large-sized deformation-induced precipitates are present in NS1 steel, with diameters exceeding 10 nm. When the coiling temperature rises to 600 °C, a significant number of fine and dispersed TiC precipitates form within the ferrite matrix, with over 90% of these precipitates having diameters smaller than 10 nm. This results in an enhancement of the precipitation strengthening effect by approximately 148 MPa. However, the grain growth that occurs at higher temperatures leads to a reduction in the contribution of fine-grain strengthening by 62 MPa.

(3) When the Ti content in steel decreased from 0.140% to 0.062%, there was no significant change in the microstructure type, which remained predominantly composed of granular bainite, ferrite, and a minor amount of pearlite. However, the quantity of the precipitated phase was notably reduced, leading to an improvement in the stability of the mechanical properties.

(4) The strength fluctuation of NS1 steel is primarily influenced by the nanoscale TiC precipitated phase. The precipitation behavior of TiC can be effectively controlled by adjusting the content of non-metallic elements, as well as the final rolling and coiling temperatures. Under the optimized processing conditions of a final rolling temperature of 860 °C and a coiling temperature of 600 °C, the optimal combination of mechanical properties and enhanced strength stability can be achieved. Under these conditions, the material exhibits a yield strength of 815 MPa, a tensile strength of 885 MPa, and an elongation of 17.5%.

Author Contributions: Conceptualization, X.G. and S.G.; methodology, C.Z., S.G. and Z.C.; software, C.Z.; validation, Z.L.; formal analysis, Z.L. and C.Z.; investigation, C.Z., L.D. and H.W.; resources, X.G.; data curation, Z.L., C.Z., L.D. and H.W.; writing—original draft preparation, Z.L.; writing—review and editing, X.G. and S.G.; visualization, C.Z., L.D. and H.W.; supervision, X.G., S.G. and Z.C.; project administration, Z.C.; funding acquisition, X.G. All authors have read and agreed to the published version of the manuscript.

Funding: This research was funded by the National Key Research and Development Program of China (No. 2022YFB3706400) and High-performance Alloy Efficient Processing Technology (N25LJR002), and the authors acknowledge the assistance.

Data Availability Statement: The raw/processed data required to reproduce these findings cannot be shared at this time, as the data are related to an ongoing study.

Conflicts of Interest: Author Zhiwei Liu was employed by the Angang Steel Co., Ltd. The remaining authors declare that the research was conducted in the absence of any commercial or financial relationships that could be construed as a potential conflict of interest.

Abbreviations

The following abbreviations are used in this manuscript:

TEM	Transmission Electron Microscopy
EBSD	Electron Back Scatter Diffraction
IPF	Inverse Pole Figure
SEM	Scanning Electron Microscope

References

1. Bikmukhametov, I.; Beladi, H.; Wang, J.; Tari, V.; Rollett, A.D.; Hodgson, P.D.; Timokhina, I. Interface characteristics and precipitation during the austenite-to-ferrite transformation of a Ti-Mo microalloyed steel. *J. Alloys Compd.* **2022**, *893*, 162224. [CrossRef]
2. Chen, S.; Li, L.; Peng, Z.; Huo, X.; Gao, J. Strain-induced precipitation in Ti microalloyed steel by two-stage controlled rolling process. *J. Mater. Res. Technol.* **2020**, *9*, 15759–15770. [CrossRef]
3. Chen, S.; Li, L.; Peng, Z.; Huo, X.; Sun, H. On the correlation among continuous cooling transformations, interphase precipitation and strengthening mechanism in Ti-microalloyed steel. *J. Mater. Res. Technol.* **2021**, *10*, 580–593. [CrossRef]
4. Shahbaz, A.; Egilmez, M.; Kannan, A.; Alnaser, A.S. Oxygen evolution reaction enhancement of copper electrodes in alkaline medium using ultrafast femtosecond laser structuring. *Int. J. Hydrogen Energy* **2024**, *52*, 2–13. [CrossRef]
5. Diaz, I.; Cano, H.; de la Fuente, D.; Chico, B.; Vega, J.M.; Morcillo, M. Atmospheric corrosion of Ni-advanced weathering steels in marine atmospheres of moderate salinity. *Corros. Sci.* **2013**, *76*, 348–360. [CrossRef]
6. Shahbaz, A.; Afaf, A.; Tahir, N.; Ullah, A.; Saim, S. Non Precious Metal Catalysts: A Fuel Cell and ORR Study of Thermally Synthesized Nickel and Platinum Mixed Nickel Nanotubes for PEMFC. *Key Eng. Mater.* **2021**, *875*, 193–199. [CrossRef]
7. Ahmad, S.; Egilmez, M.; Abuzaid, W.; Mustafa, F.; Kannan, A.M.; Alnaser, A.S. Efficient medium entropy alloy thin films as bifunctional electrodes for electrocatalytic water splitting. *Int. J. Hydrogen Energy* **2024**, *52*, 1428–1439. [CrossRef]
8. Gong, P.; Palmiere, E.J.; Rainforth, W.M. Thermomechanical processing route to achieve ultrafine grains in low carbon microalloyed steels. *Acta Mater.* **2016**, *119*, 43–54. [CrossRef]
9. Han, Y.; Shi, J.; Xu, L.; Cao, W.Q.; Dong, H. Effect of hot rolling temperature on grain size and precipitation hardening in a Ti-microalloyed low-carbon martensitic steel. *Mater. Sci. Eng. A* **2012**, *553*, 192–199. [CrossRef]
10. He, P.; Hu, H.; Wang, W.; Wang, L.; Xu, G. On the correlation among isothermal transformation, interphase precipitation behaviour and elements partitioning in Ti–Mo microalloyed steel. *J. Mater. Res. Technol.* **2024**, *29*, 1901–1910. [CrossRef]
11. Hu, J.; Du, L.-X.; Wang, J.-J.; Xie, H.; Gao, C.-R.; Misra, R.D.K. Structure–mechanical property relationship in low carbon microalloyed steel plate processed using controlled rolling and two-stage continuous cooling. *Mater. Sci. Eng. A* **2013**, *585*, 197–204. [CrossRef]
12. Huang, Y.; Han, J.; Liu, W.; Li, F.; Zhao, A.; Liu, Y. Effect of the Final Rolling Temperature on the Precipitation Behavior and Toughening Mechanism of Nanoparticles in Ferritic Steel. *J. Mater. Eng. Perform.* **2020**, *29*, 1724–1731. [CrossRef]
13. Huo, X.; Li, L.; Peng, Z.; Chen, S. Effects of TMCP Schedule on Precipitation, Microstructure and Properties of Ti-microalloyed High Strength Steel. *J. Iron Steel Res. Int.* **2016**, *23*, 593–601. [CrossRef]
14. Jia, J.; Liu, Z.; Cheng, X.; Du, C.; Li, X. Development and optimization of Ni-advanced weathering steel: A review. *Corros. Commun.* **2021**, *2*, 82–90. [CrossRef]
15. Kobayashi, Y.; Takahashi, J.; Kawakami, K. Effects of dislocations on the early stage of TiC precipitation kinetics in ferritic steel: A comparative study with and without a pre-deformation. *Acta Mater.* **2019**, *176*, 145–154. [CrossRef]
16. Koo, B.S.; Lee, C.W.; Lim, Y.H. A study on Nb-V microalloyed steel for 460 MPa grade H-section columns. *J. Constr. Steel Res.* **2020**, *170*, 106112. [CrossRef]
17. Li, G.; Guo, X.; Li, T.; Wang, S. Development of low-cost weathering steel for photovoltaic supports. *Metall. Res. Technol.* **2023**, *120*, 115. [CrossRef]
18. Li, P.; Sun, H.L.; Jiao, X.Y.; Ding, H. Achieving an ultrahigh yield strength of 1.5 GPa in warm-rolled lightweight steel via synergistic multiplication of precipitation and dislocations. *Mater. Charact.* **2024**, *214*, 114097. [CrossRef]
19. Li, Z.; Liu, L.; Xue, Q.; Wu, C.; Lu, F.; Zhao, Z. Study on microstructure characteristics and hole expansion mechanism of Ti–Nb–V microalloyed 900 MPa hot-rolled ferrite-bainite high hole expansion steel. *J. Mater. Res. Technol.* **2024**, *33*, 7469–7481. [CrossRef]
20. Lian, Y.; Huang, J.; Zhang, J.; Zhang, C.; Gao, W.; Zhao, C. Effect of 0.2 and 0.5% Ti on the microstructure and mechanical properties of 13Cr supermartensitic stainless steel. *J. Mater. Eng. Perform.* **2015**, *24*, 4253–4259. [CrossRef]

21. Liang, Y.; Li, G.; Liu, L.; Jiang, H.; Wang, X.; Cao, J.; Jiang, J.; Shao, W.; Zhen, L. Influence of Cu and Ti microalloying on the multiscale microstructure evolution and mechanical properties of 7xxx alloys. *J. Mater. Sci. Technol.* **2025**, *223*, 235–251. [CrossRef]
22. Mao, X.; Huo, X.; Sun, X.; Chai, Y. Strengthening mechanisms of a new 700MPa hot rolled Ti-microalloyed steel produced by compact strip production. *J. Mater. Process. Technol.* **2010**, *210*, 1660–1666. [CrossRef]
23. Chen, C.; Yang, J.; Chen, C.; Chen, S. Microstructural characterization and strengthening behavior of nanometer sized carbides in Ti–Mo microalloyed steels during continuous cooling process. *Mater. Charact.* **2016**, *114*, 18–29. [CrossRef]
24. Natarajan, V.V.; Challa, V.S.A.; Misra, R.D.K.; Sidorenko, D.M.; Mulholland, M.D.; Manohar, M.; Hartmann, J.E. The determining impact of coiling temperature on the microstructure and mechanical properties of a titanium-niobium ultrahigh strength microalloyed steel: Competing effects of precipitation and bainite. *Mater. Sci. Eng. A* **2016**, *665*, 1–9. [CrossRef]
25. Patra, P.K.; Sam, S.; Singhai, M.; Hazra, S.S.; Janaki Ram, G.D.; Bakshi, S.R. Effect of Coiling Temperature on the Microstructure and Mechanical Properties of Hot-Rolled Ti–Nb Microalloyed Ultra High Strength Steel. *Trans. Indian Inst. Met.* **2017**, *70*, 1773–1781. [CrossRef]
26. Peng, T.; Lian, Z.; Zhang, Y.; He, B.; Hu, X.; Zhu, T.; Jiang, B. Enhancing strength of an ultra-low-carbon weathering steel to 700 MPa by adjusting Ti content. *J. Iron Steel Res. Int.* **2023**, *30*, 2494–2504. [CrossRef]
27. Peng, Z.; Li, L.; Chen, S.; Huo, X.; Gao, J. Isothermal precipitation kinetics of carbides in undercooled austenite and ferrite of a titanium microalloyed steel. *Mater. Des.* **2016**, *108*, 289–297. [CrossRef]
28. Peng, Z.; Li, L.; Gao, J.; Huo, X. Precipitation strengthening of titanium microalloyed high-strength steel plates with isothermal treatment. *Mater. Sci. Eng. A* **2016**, *657*, 413–421. [CrossRef]
29. Rancel, L.; Gómez, M.; Medina, S.F. Influence of Microalloying Elements (Nb, V, Ti) on Yield Strength in Bainitic Steels. *Steel Res. Int.* **2008**, *79*, 947–953. [CrossRef]
30. Saastamoinen, A.; Kaijalainen, A.; Porter, D.; Suikkanen, P.; Yang, J.-R.; Tsai, Y.-T. The effect of finish rolling temperature and tempering on the microstructure, mechanical properties and dislocation density of direct-quenched steel. *Mater. Charact.* **2018**, *139*, 1–10. [CrossRef]
31. Shen, Y.F.; Wang, C.M.; Sun, X. A micro-alloyed ferritic steel strengthened by nanoscale precipitates. *Mater. Sci. Eng. A* **2011**, *528*, 8150–8156. [CrossRef]
32. Song, L.; Gao, X.; Wang, M.; Xue, Q.; Misra, R.D.K.; Li, J.; Wu, H.; Du, L. Study on Flow Behavior and Processing Maps of High-Ti Low-C Microalloyed Steel during Hot Compression. *Steel Res. Int.* **2021**, *92*, 2100009. [CrossRef]
33. Song, L.Y.; Gao, X.H.; Xue, Q.H.; Li, J.B.; Wu, H.Y. Effect of Cooling Rate and Coiling Temperature on Microstructure and Precipitation Behavior of a 700 MPa Weathering Steel. *J. Mater. Eng. Perform.* **2022**, *31*, 10225–10236. [CrossRef]
34. Soto, R.; Saikaly, W.; Bano, X.; Issartel, C.; Rigaut, G.; Charai, A. Statistical and theoretical analysis of precipitates in dual-phase steels microalloyed with titanium and their effect on mechanical properties. *Acta Mater.* **1999**, *47*, 3475–3481. [CrossRef]
35. Tian, Y.; Yu, H.; Zhou, T.; Wang, K.; Zhu, Z. Revealing morphology rules of MX precipitates in Ti-V-Nb multi-microalloyed steels. *Mater. Charact.* **2022**, *188*, 111919. [CrossRef]
36. Dong, J.; Liu, C.; Li, C.; Guo, Q.; Li, H. Effects of two different types of MX carbonitrides on austenite growth behavior of Nb-V-Ti microalloyed ultra-high strength steel. *Fus. Eng. Des.* **2017**, *125*, 415–422. [CrossRef]
37. Wang, Y.; Che, Z.; Chen, Y.; Yang, S.; Xue, Q.; Bai, J. Influence mechanism of solution temperature on microstructure evolution and tensile properties of Ti microalloyed high strength steel CGLC700. *J. Mater. Res. Technol.* **2024**, *30*, 2936–2944. [CrossRef]
38. Wang, Z.; Mao, X.; Yang, Z.; Sun, X.; Yong, Q.; Li, Z.; Weng, Y. Strain-induced precipitation in a Ti micro-alloyed HSLA steel. *Mater. Sci. Eng. A* **2011**, *529*, 459–467. [CrossRef]
39. Wei, F.-G.; Hara, T.; Tsuzaki, K. High-resolution transmission electron microscopy study of crystallography and morphology of TiC precipitates in tempered steel. *Philos. Mag.* **2004**, *84*, 1735–1751. [CrossRef]
40. Woo Kim, Y.; Hong, S.-G.; Huh, Y.-H.; Lee, C.S. Role of rolling temperature in the precipitation hardening characteristics of Ti–Mo microalloyed hot-rolled high strength steel. *Mater. Sci. Eng. A* **2014**, *615*, 255–261. [CrossRef]
41. Wu, W.; Cheng, X.; Hou, H.; Liu, B.; Li, X. Insight into the product film formed on Ni-advanced weathering steel in a tropical marine atmosphere. *Appl. Surf. Sci.* **2018**, *436*, 80–89. [CrossRef]
42. Zhang, B.; Liu, W.; Sun, Y.; Yang, W.; Chen, L.; Xie, J.; Li, W. Corrosion behavior of the 3 wt.% Ni weathering steel with replacing 1 wt.% Cr in the simulated tropical marine atmospheric environment. *J. Phys. Chem. Solids* **2023**, *175*, 111221. [CrossRef]
43. Zhang, K.; Zhang, T.; Wei, H.; Zhang, M.; Zhao, S.; Li, J.; Pan, H.; Yang, G.; Zhao, P. Effect of isothermal holding time on microstructure, precipitates and hardness of Ti–V–Mo microalloyed steel during coiling process. *J. Mater. Res. Technol.* **2024**, *32*, 753–761. [CrossRef]
44. Zhang, K.; Zhang, T.; Zhang, M.; Chen, Z.; Pan, H.; Yang, G.; Cao, Y.; Li, Z.; Zhang, X. Hot deformation behavior, dynamic recrystallization mechanism and processing maps of Ti–V microalloyed high strength steel. *J. Mater. Res. Technol.* **2023**, *25*, 4201–4215. [CrossRef]
45. Zheng, Y.; Wang, K.; Yang, Q.; Lin, Y.; Zhu, L.; Wu, X.; Han, B.; Wang, B.; Zhang, D.; Feng, J.; et al. Research on the strengthening mechanism of Nb–Ti microalloyed ultra low carbon IF steel. *J. Mater. Res. Technol.* **2024**, *30*, 5785–5803. [CrossRef]

46. Zhou, F.; Liu, L.; Chu, X.; Zhao, Y.; Zhao, Z. Strengthening mechanism and precipitation behavior of advanced ultrahigh-strength titanium microalloy weathering steels for photovoltaic support. *Mater. Charact.* **2024**, *208*, 113660. [CrossRef]
47. Zhu, C.; Gao, X.; Zhu, C.; Liu, Z.; Fu, Y.; Li, W.; Du, L.; Wu, H. Insight into the excellent corrosion resistance of a new type of weathering steel in high chloride environment by dissolution-diffusion-deposition-synergy model. *Constr. Build. Mater.* **2025**, *485*, 141901. [CrossRef]